Supplementary Information

Near-planar light outcoupling structures with a finite lateral dimension for ultra-efficient and crosstalk-free OLED displays

MinJae Kim[1], Junho Kim[2], and Seunghyup Yoo[2*]

[1] Department of Materials Science and Engineering, Korea Advanced Institute of Science and Technology, Daejeon 34141, South Korea

[2] School of Electrical Engineering, Korea Advanced Institute of Science and Technology, Daejeon 34141, South Korea

* Corresponding author. Email: syoo_ee@kaist.ac.kr (S. Yoo)

Table of Contents

Supplementary Notes 1 – 3

Supplementary Figures 1 – 27

Supplementary Note 1. Angular Transfer Weight

The Hertzian dipole oscillator-based formalism constructed by Chance, Prock, and Silvey (CPS model) postulates an infinite-plane configuration of each layer within the stratified structure.[1–3] Therefore, the CPS model is incompatible for evaluating power concentrated within finite reception apertures. Hence, time-consuming trans-scale Monte-Carlo-type ray-tracing simulations have been used to estimate the power fetching from and to finite emission and reception apertures (EA and RA, respectively).

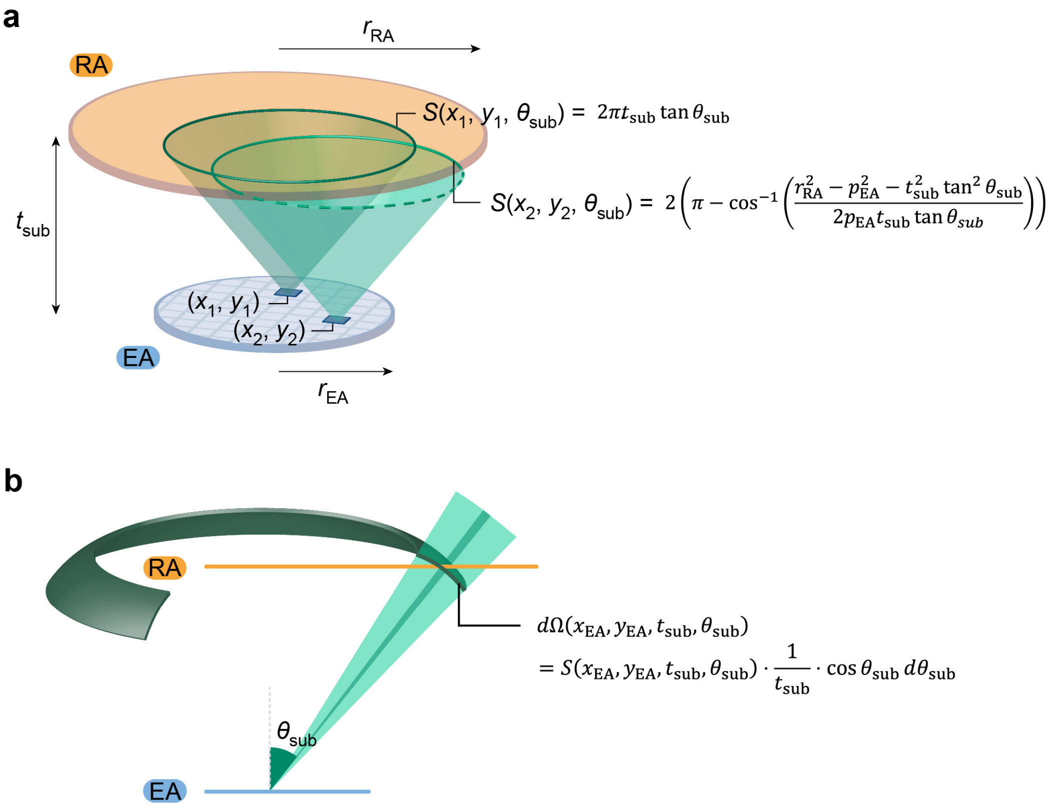

Supplementary Figure 1. Schematic diagram of the RA, EA, and the ray cones. (a) The length of the circumference of the ray cone that comes within the RA, (b) The diminutive solid angle defined by the circumference.

Here, we conceived angular transfer weight (ATW) to analytically estimate the interaperture power delivery. For brevity, we assume, but not limited to, circular apertures parallel to each other with a shared centrosymmetric axis. For a diminutive light-emitting area $dA = dxdy$ centered at $(x_{\mathrm{EA}}, y_{\mathrm{EA}}, 0)$ and a given uniformity of the planar source and random azimuthal distribution of the transition dipole moment within the emission layer (EML), rays with a polar angle of θ_{sub} forms a 'ray cone' with its centrosymmetric axis parallel to the z-axis. The reachability of the rays to the RA depends on the position of dA and θ_{sub}. As shown in **Supplementary Fig. 1**, a part of the rays emitted from dA may not reach the RA.

To take this partial power fetching into account, the length of the circumference of the ray cone that comes within the RA, $S(p_{\mathrm{EA}}, t_{\mathrm{sub}}, \theta_{\mathrm{sub}})$, is defined, where $p_{\mathrm{EA}} = \sqrt{x_{\mathrm{EA}}^2 + y_{\mathrm{EA}}^2}$. The length S is estimated as follows:

$$S(x_{\mathrm{EA}}, y_{\mathrm{EA}}, t_{\mathrm{sub}}, \theta_{\mathrm{sub}}) = \begin{cases} 2\pi t_{\mathrm{sub}} \tan\theta_{\mathrm{sub}} & (\text{if } |p_{\mathrm{EA}}| + t_{\mathrm{sub}} \tan\theta_{\mathrm{sub}} \leq r_{\mathrm{RA}}) \\ 0 & (\text{if } t_{\mathrm{sub}} \tan\theta_{\mathrm{sub}} - |p_{\mathrm{EA}}| \geq r_{\mathrm{RA}}) \\ 2\left(\pi - \cos^{-1}\left(\dfrac{r_{\mathrm{RA}}^2 - p_{\mathrm{EA}}^2 - t_{\mathrm{sub}}^2 \tan^2\theta_{\mathrm{sub}}}{2 p_{\mathrm{EA}} t_{\mathrm{sub}} \tan\theta_{sub}}\right)\right) & (\text{otherwise}) \end{cases}$$

Then, the solid angle of the ray cone shell ($d\Omega$) defined by $d\theta_{\mathrm{sub}}$ is given by the following equation. (See **Supplementary Fig. 1**)

$$d\Omega(x_{\mathrm{EA}}, y_{\mathrm{EA}}, t_{\mathrm{sub}}, \theta_{\mathrm{sub}}) = S(x_{\mathrm{EA}}, y_{\mathrm{EA}}, t_{\mathrm{sub}}, \theta_{\mathrm{sub}}) \cdot \frac{1}{t_{\mathrm{sub}}} \cdot \cos\theta_{\mathrm{sub}}\, d\theta_{\mathrm{sub}}$$

Then, the power delivered into $d\Omega$ from the whole EA (dP_{RA}) is given by the following equation.

$$\begin{aligned} dP_{\mathrm{RA}} &= \frac{1}{A_{\mathrm{EA}}} \iint\limits_{(x_{\mathrm{EA}}, y_{\mathrm{EA}}) \in \mathrm{EA}} I_{\mathrm{to-sub}}(\theta_{\mathrm{sub}})\, d\Omega dx_{\mathrm{EA}} dy_{\mathrm{EA}} \\ &= \frac{1}{t_{\mathrm{sub}} A_{\mathrm{EA}}} \iint\limits_{(x_{\mathrm{EA}}, y_{\mathrm{EA}}) \in \mathrm{EA}} I_{\mathrm{to-sub}}(\theta_{\mathrm{sub}})\, S(x_{\mathrm{EA}}, y_{\mathrm{EA}}, t_{\mathrm{sub}}, \theta_{\mathrm{sub}}) \cos\theta_{\mathrm{sub}}\, dx_{\mathrm{EA}} dy_{\mathrm{EA}} d\theta_{\mathrm{sub}} \end{aligned}$$

Therefore, we define the ATW as follows, so that the total power delivered to the RA can be estimated by $P_{\mathrm{RA}} = \frac{1}{t_{\mathrm{sub}} A_{\mathrm{EA}}} \int I_{\mathrm{to-sub}}(\theta_{\mathrm{sub}}) \cdot \mathrm{ATW}(\theta_{\mathrm{sub}}) d\theta_{\mathrm{sub}}$.

$$\mathrm{ATW}(\theta_{\mathrm{sub}}) = \iint_{(x_{\mathrm{EA}}, y_{\mathrm{EA}}) \in \mathrm{EA}} S(x_{\mathrm{EA}}, y_{\mathrm{EA}}, \theta_{\mathrm{sub}}) \cdot \cos\theta_{\mathrm{sub}}\, dx_{\mathrm{EA}} dy_{\mathrm{EA}}$$

Supplementary Note 2. Optical structure design

We first postulate that the optimal LOS topography $z_{\mathrm{LOS}}(x_{\mathrm{LOS}}, y_{\mathrm{LOS}})$ is centrosymmetric if the EA and RA share a common centrosymmetric axis along the z-direction. Then, $z_{\mathrm{LOS}}(x_{\mathrm{LOS}}, y_{\mathrm{LOS}})$ is defined by a compressed function $z_{\mathrm{LOS}}(r)$, which is comprised of alternating C-edges and S-edges.

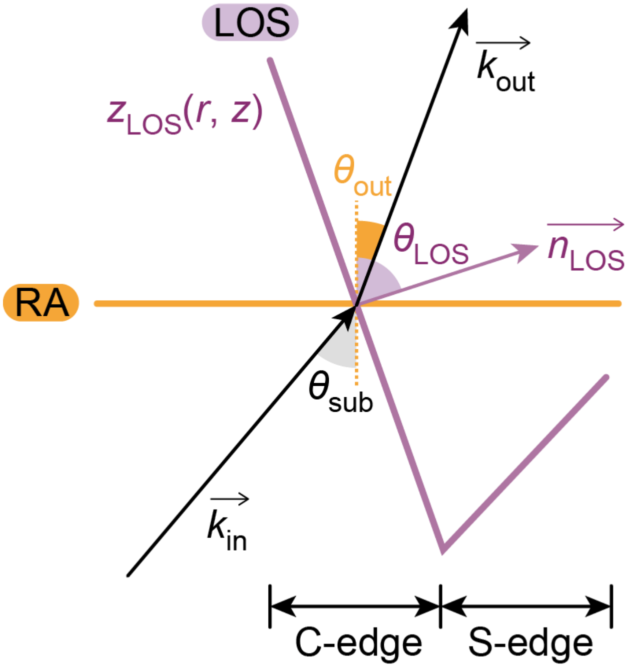

Supplementary Figure 2. schematic ray diagram emitted with a polar angle of θ_{sub} from the EA.

First, the S-edges are defined to be parallel to the vector from the origin to the starting point of the S-edges, inheriting the ‘flat’ edge of the PS-LOS. Second, the C-edges are defined by connecting diminutive linear strokes which slope $(\frac{d}{dr} z_{\mathrm{LOS}}(r, z))$ is optimized by the following method. For a diminutive light-emitting area $dA_{\mathrm{EA}} = dx_{\mathrm{EA}} dy_{\mathrm{EA}}$ centered at $\overrightarrow{P_{\mathrm{EA}}} = (x_{\mathrm{EA}}, y_{\mathrm{EA}}, 0)$ and an infinitesimal part of the LOS surface dA_{LOS} centered at $\overrightarrow{P_{\mathrm{LOS}}} = (x_{\mathrm{LOS}}, y_{\mathrm{LOS}}, z(x_{\mathrm{LOS}}, y_{\mathrm{LOS}}))$ with the normal vector given by the following equation.

$$\overrightarrow{n_{\mathrm{LOS}}}\left(\overrightarrow{P_{\mathrm{LOS}}}\right)=\frac{1}{\sqrt{\left(\frac{\partial z_{\mathrm{LOS}}}{\partial x_{\mathrm{LOS}}}\right)^2+\left(\frac{\partial z_{\mathrm{LOS}}}{\partial y_{\mathrm{LOS}}}\right)^2+1}}\left(-\frac{\partial z_{\mathrm{LOS}}}{\partial x_{\mathrm{LOS}}},-\frac{\partial z_{\mathrm{LOS}}}{\partial y_{\mathrm{LOS}}},1\right)$$

Then, for the incident wavevector $\overrightarrow{k_{\mathrm{in}}}=\frac{2\pi n_{\mathrm{sub}}}{\lambda}\frac{\overrightarrow{P_{\mathrm{LOS}}}-\overrightarrow{P_{\mathrm{EA}}}}{\left|\overrightarrow{P_{\mathrm{LOS}}}-\overrightarrow{P_{\mathrm{EA}}}\right|}$, in-plane and out-of-plane parts of the wavevector are respectively given by $\overrightarrow{k_{\mathrm{in},\perp}}=(\overrightarrow{k_{\mathrm{in}}}\cdot\overrightarrow{n_{\mathrm{LOS}}})\overrightarrow{n_{\mathrm{LOS}}}$ and $\overrightarrow{k_{\mathrm{in},\parallel}}=\left(\overrightarrow{n_{\mathrm{LOS}}}\times\overrightarrow{k_{\mathrm{in}}}\right)\times\overrightarrow{n_{\mathrm{LOS}}}$. The refractive wavevector ($\overrightarrow{k_{\mathrm{out}}}$) therefore is the sum of its in-plane and out-of-plane parts given by the following equations.

$$\overrightarrow{k_{\mathrm{out}}}=\overrightarrow{k_{\mathrm{out},\perp}}+\overrightarrow{k_{\mathrm{out},\parallel}}$$

$$\overrightarrow{k_{\mathrm{out},\parallel}}=\overrightarrow{k_{\mathrm{in},\parallel}}$$

$$\left|\overrightarrow{k_{\mathrm{out}}}\right|=\frac{1}{n_{\mathrm{sub}}}\left|\overrightarrow{k_{\mathrm{in}}}\right|$$

The transmittance of the rays emitted from dA_{EA} and transmitted through dA_{LOS} is given by the following equation, where t is the Fresnel transmission coefficient.

$$T=|t|^2\cdot\left(\frac{\mathrm{Re}\left|\overrightarrow{k_{\mathrm{out},\perp}}\right|}{\mathrm{Re}\left|\overrightarrow{k_{\mathrm{in},\perp}}\right|}\right)$$

Provided uniformity of the planar source and random azimuthal distribution of the transition dipole moment within the emission layer (EML), the power of rays emitted from a unit area centered at $(x_{\mathrm{EA}},y_{\mathrm{EA}},0)$ on the EA with a polar angle of θ_{sub} transmitted to air through dA_{OS} is given by the following equation.

$$dP(dA_{\mathrm{EA}},dA_{\mathrm{LOS}},\theta_{\mathrm{sub}})=\frac{1}{A_{\mathrm{EA}}}\cdot T\cdot I_{\mathrm{to-sub}}(\theta_{\mathrm{sub}})\sin\theta_{\mathrm{sub}}\,d\theta_{\mathrm{sub}}$$

Given the design philosophy of the S-edges, rays that come from dA_{EA} centered at $(x_{\mathrm{EA}},y_{\mathrm{EA}},0)$ where $x_{\mathrm{EA}}<0$ would be shadowed by the S-edges in advance to reach the intended surfaces on the C-edges. Moreover, the rays outcoupled with its $\theta_{\text{out}} > \tan^{-1}\left(\frac{r}{z_{\text{LOS}}(r)}\right)$ would be recoupled into the LOS by adjacent S-edges. Taking into account all these geometric constraints, the total power effectively outcoupled into the air is written by the following equation.

$$P_{\text{out}} = \iint_{\theta_{\text{out}} \le \tan^{-1}\left(\frac{r}{z_{\text{LOS}}(r)}\right)} \iint_{(x_{\text{EA}} \ge 0, y_{\text{EA}}) \in \text{EA}} W(\theta_{\text{out}}) dx_{\text{EA}} dy_{\text{EA}} dP(dA_{\text{EA}}, dA_{\text{LOS}}, \theta_{\text{sub}}) \sin\theta_{\text{out}}\, d\theta_{\text{out}}$$

Then the optimal $\overrightarrow{n_{\text{LOS}}}(\overrightarrow{P_{\text{LOS}}})$ for the C-edge part can be determined by selecting $\overrightarrow{n_{\text{LOS}}}(\overrightarrow{P_{\text{LOS}}})$ such that gives the maximum $P_{\text{out}} = \int_{\substack{(x_{\text{EA}} \ge 0, y_{\text{EA}}) \in \text{EA} \\ \theta_{\text{out}} \le \tan^{-1}\left(\frac{r}{z_{\text{LOS}}(r)}\right)}} I_{\text{out}}(\theta_{\text{out}}) \cdot \sin\theta_{\text{out}} \cdot W(\theta_{\text{out}})\, d\theta_{\text{out}}$. Therefore, by combining the C-edges defined by the aforementioned method and S-edges parallel to $\overrightarrow{P_{\text{LOS}}}$, the cross-section of a centrosymmetric LOS with a given t_{in} is defined.

Supplementary Note 3. Mismatch between r_{LOS} and r_{RA}.

The sequential approach explained in **Supplementary Note 2** is based on the ray redirecting capability of refraction at the LOS-air interface. Therefore, this approach inevitably bears a limitation in caliber in refraction, mainly delimited by the critical angle at the interface, especially in the case of some weight functions like lowpass functions. To illustrate this intuitively and succinctly, we consider 2-dimensional EA, RA, and LOS, as shown in **Supplementary Fig. 3**. The polar angle of the incident ray, outcoupled ray, and normal to the LOS surface ($\overrightarrow{n_{\mathrm{LOS}}}$) are θ_{sub} (it should be noted that the EA and RA are posited to be parallel for brevity), θ_{out}, and θ_{LOS}, respectively.

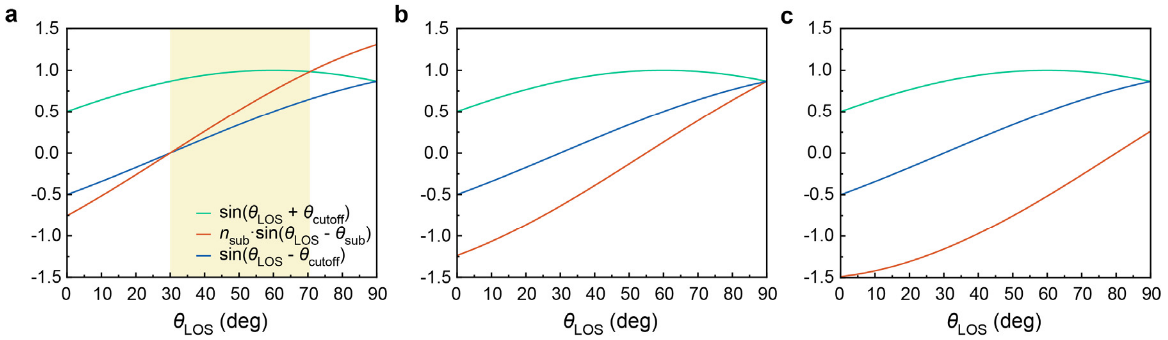

Supplementary Figure 3. Availability of the LOS topography for the lowpass weighting function. In the yellow region, in which there exists at least one ray that satisfies $\sin(\theta_{\mathrm{LOS}} - \theta_{\mathrm{cutoff}}) \le n_{\mathrm{sub}} \cdot \sin(\theta_{\mathrm{LOS}} - \theta_{\mathrm{sub}}) \le \sin(\theta_{\mathrm{LOS}} + \theta_{\mathrm{cutoff}})$, the normal of the LOS exists. (a) $\theta_{\mathrm{sub}} = 30°$, (b) $\theta_{\mathrm{sub}} = 55°$, (c) $\theta_{\mathrm{sub}} = 80°$.

As an example, a lowpass function with a cutoff angle of θ_{cutoff} is considered to epitomize the mismatch between r_{LOS} and r_{RA}. In this case, $\overrightarrow{n_{\mathrm{LOS}}}$ exists only if there is at least one possible θ_{sub} such that makes $\theta_{\mathrm{out}} \le \theta_{\mathrm{cutoff}}$. Mathematically, this geometric constraint in the existence of the $\overrightarrow{n_{\mathrm{LOS}}}$ is represented by the following equation.

$$\sin(\theta_{\mathrm{LOS}} - \theta_{\mathrm{cutoff}}) \le n_{\mathrm{sub}} \cdot \sin(\theta_{\mathrm{LOS}} - \theta_{\mathrm{sub}}) \le \sin(\theta_{\mathrm{LOS}} + \theta_{\mathrm{cutoff}})$$

Therefore, the availability of the $\theta_{\mathrm{LOS}} = \pi - \tan^{-1}\left(\frac{dz_{\mathrm{LOS}}}{dr}\right)$ is delimited by the minimal θ_{sub} (the polar angle of the incident ray that is emanated from the one end of the EA to the end at the same side of the RA). The yellow region in **Supplementary Fig. 3** indicates the window of feasible θ_{LOS}. As can be seen in **Supplementary Fig. 8**, a large n_{sub} extends the available window of r on which $\theta_{\mathrm{LOS}}(r)$ exists.

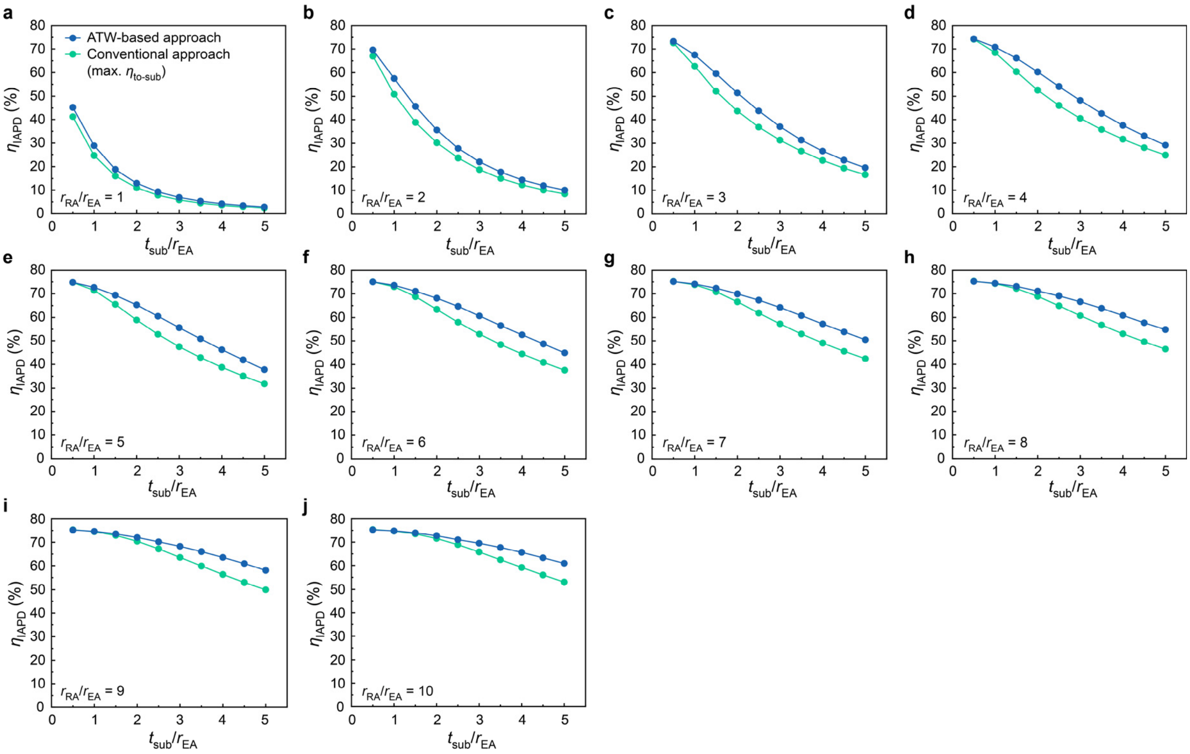

Supplementary Figure 4. Simulated ratio of power emitted from the EML to the power reaching to the RA. The aperture radius ratio ($r_{\text{RA}}/r_{\text{EA}}$) was set to be (a) 1, (b) 2, (c) 3, (d) 4, (e) 5, (f) 6, (g) 7, (h) 8, (i) 9, and (j) 10. The ATW-based and conventional approach are designed to find ($d_{\text{ETL}}, d_{\text{HTL}}$) which maximizes $\int_0^{\pi/2} I_{\text{to-sub}}(\theta_{\text{sub}}, d_{\text{ETL}}, d_{\text{HTL}}) \cdot \text{ATW}(\theta_{\text{sub}}, \frac{r_{\text{RA}}}{r_{\text{EA}}}, \frac{t_{\text{sub}}}{r_{\text{EA}}})\, d\theta_{\text{sub}}$ and $\int_0^{\pi/2} I_{\text{to-sub}}(\theta_{\text{sub}}, d_{\text{ETL}}, d_{\text{HTL}}) \cdot \sin\theta_{\text{sub}} d\theta_{\text{sub}}$, respectively. For all geometry, the OLEDs designed with the ATW-based approach always yielded in more power concentrated within the RA compared to those based on conventional approach which maximizes $\eta_{\text{to-sub}}$.

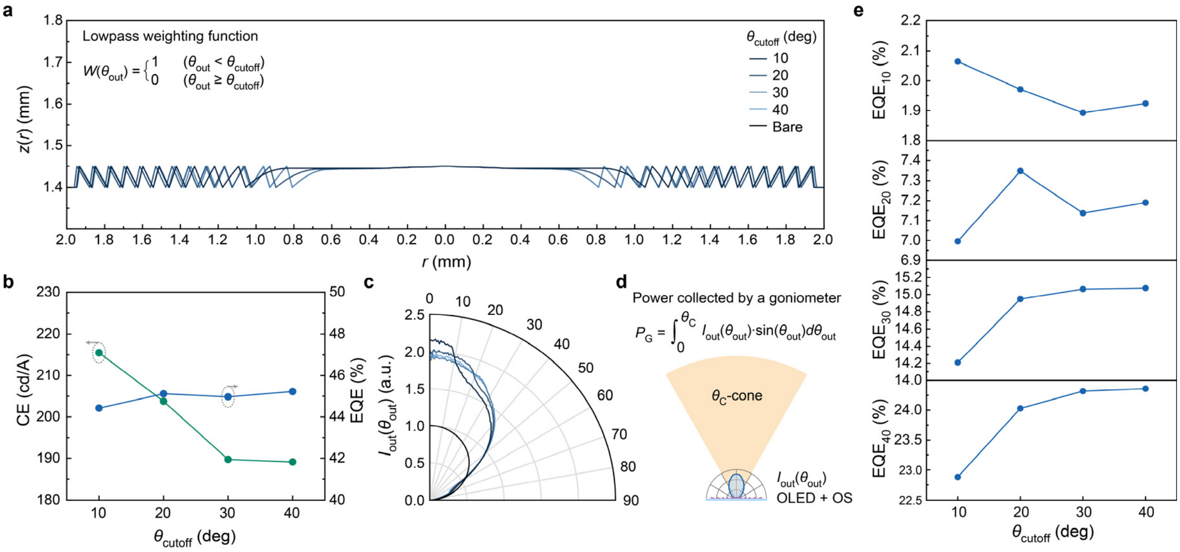

Supplementary Figure 5. The impact of the weighting function in the LOS design revealed by trans-scale optical simulations. (a) Cross-sections of the LP-LOSs designed with lowpass functions with different cutoff angles (θ_P). (b, c) Performances of OLEDs with LP-LOSs with different θ_P. Here, r_{RA}/r_{EA}, t_{sub}/r_{EA}, and n_sub were 2, 1.4, and 1.51, respectively. EQE and CE (b), and angular emission intensities (c) of the OLEDs with different θ_P. (d) Schematic diagram of the method to estimate $\mathrm{EQE}_{\theta_\mathrm{C}}$. e, $\mathrm{EQE}_{\theta_\mathrm{C}}$ of the OLEDs with LP-LOS designed with different θ_C.

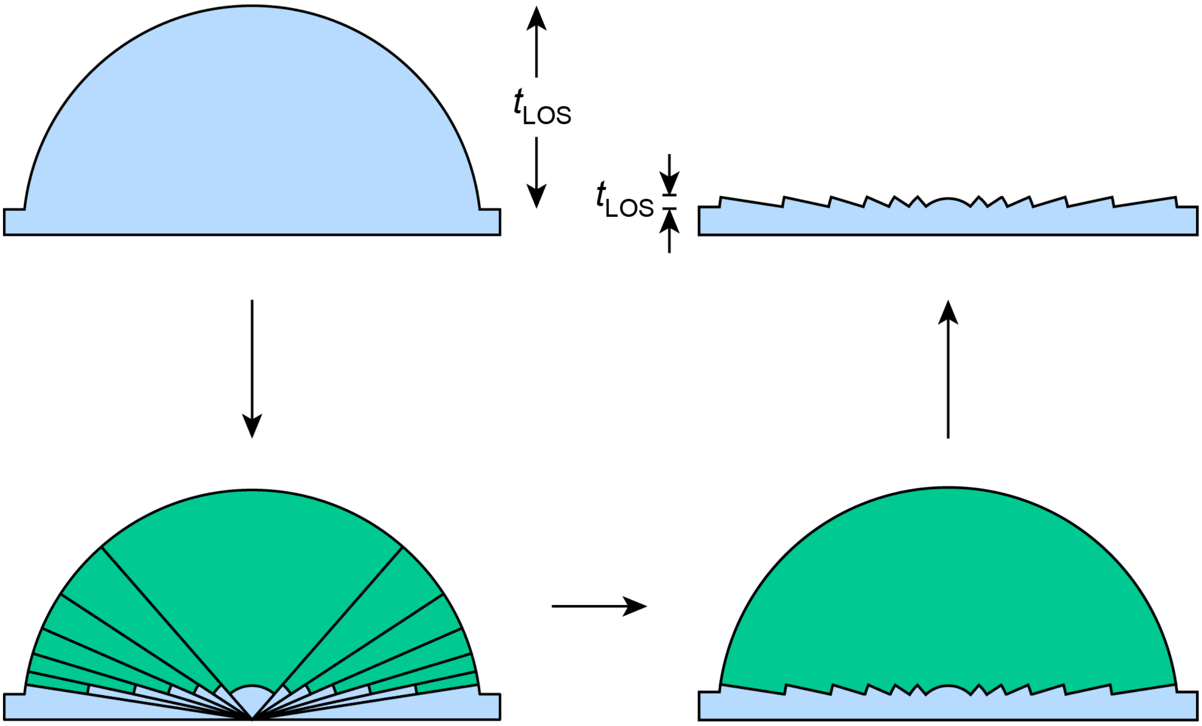

Supplementary Figure 6. Design principle of the PS-LOS. A macroscale half-ball lens is dissected radially to find curved surfaces with larger curvatures at no expense of incidence angle from the point source. Then, an ultrathin optical structure is enabled by excising the bulky part (green region). This enables an optical structure with a smaller t_{LOS} while maintaining the identical optical power for the point source.

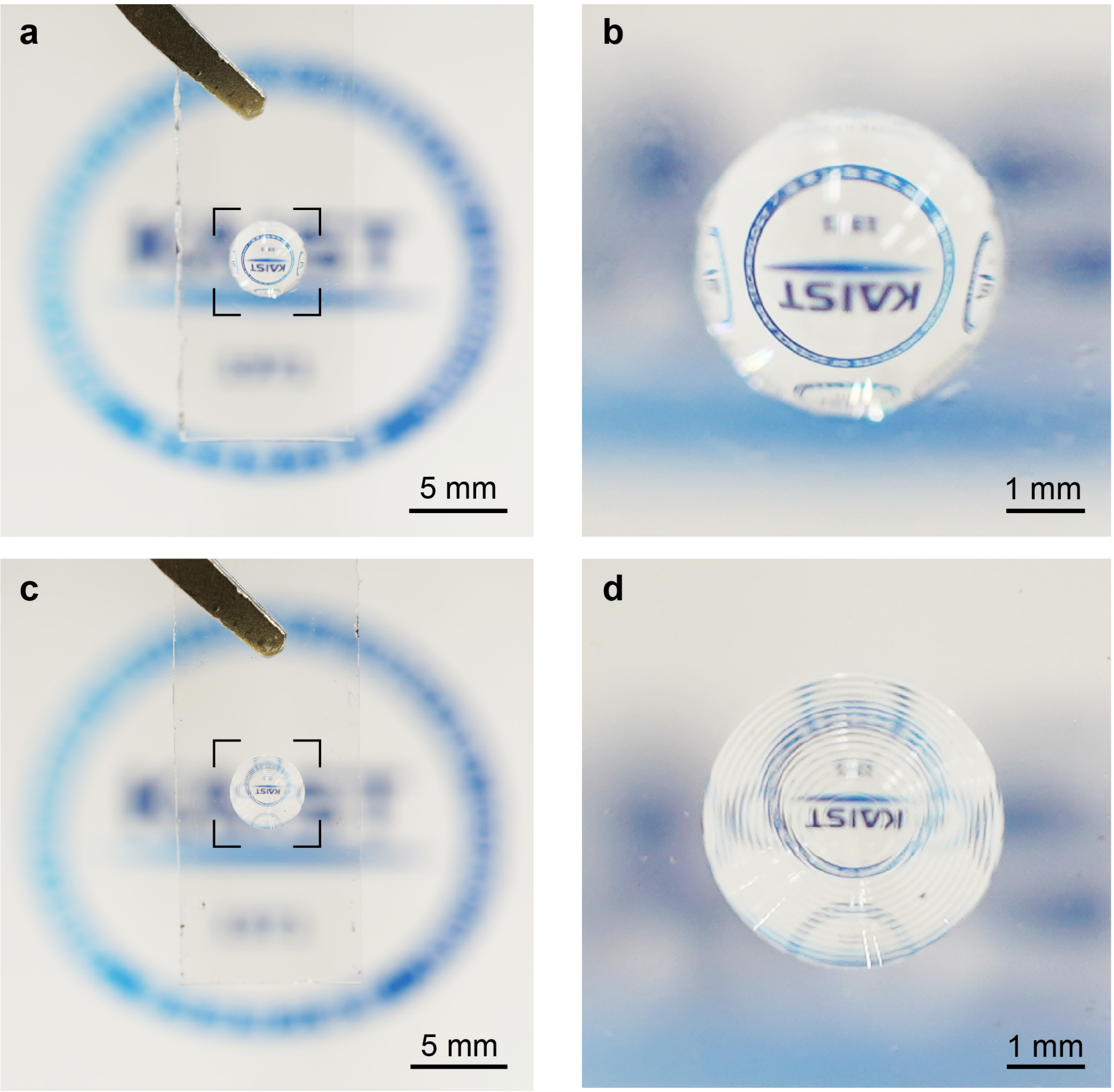

Supplementary Figure 7. Optical equivalence of the macroscale half-ball and PS-LOS. (a) Macroscale half-ball ($r_{\mathrm{LOS}} = 2$ mm), (b) its close-up image, (c) PS-LOS ($r_{\mathrm{LOS}} = 1.912$ mm, $t_{\mathrm{LOS}} = 50$ µm, $r_{\mathrm{EA}} = 1$ mm, $t_{\mathrm{sub}} = 1.4\,mm$, and $n_{\mathrm{sub}} = 1.51$.), and (d) its close-up image. The macroscale half-ball made of N-BK7 (refractive index of 1.51) was optically attached onto a glass substrate (refractive index of 1.51) with NOA74 (refractive index of 1.51).

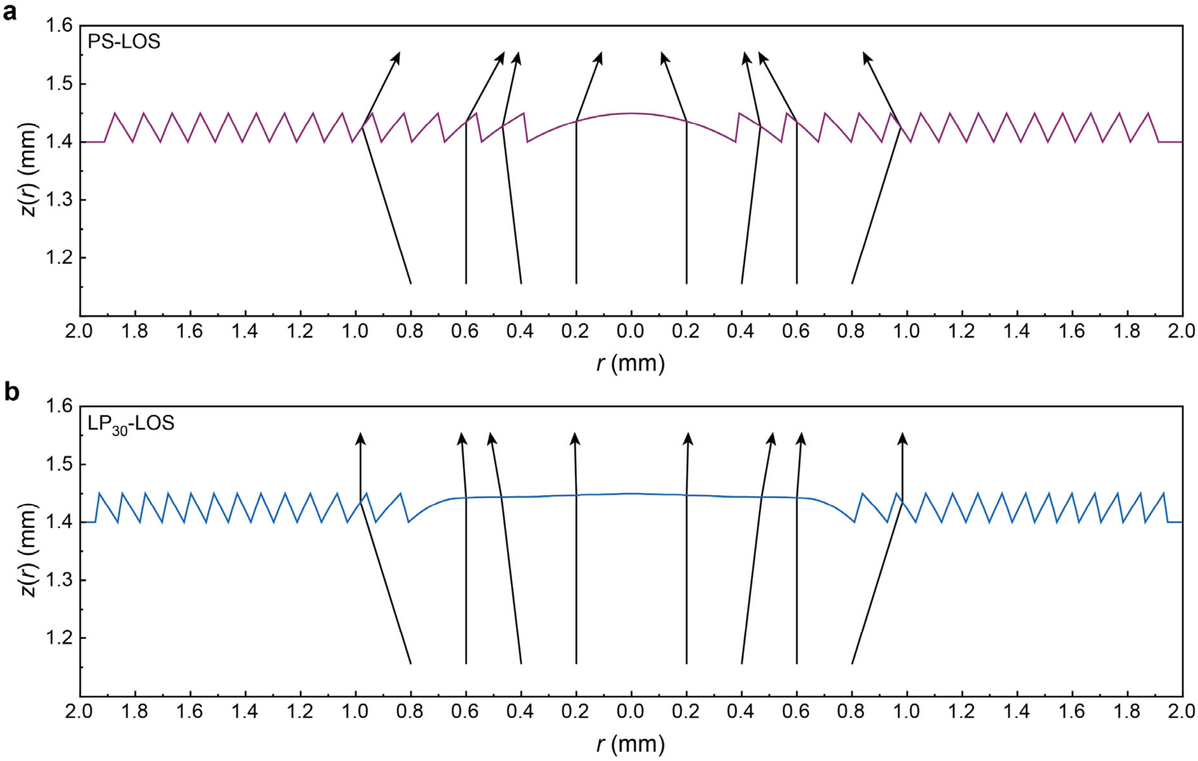

Supplementary Figure 8. Ray diagram for (a) PS-LOS and (b) LP$_{30}$-LOS. In the case of PS-LOS, rays emanated from a planar source with small θ_{sub} are refracted into larger θ_{out}, mainly because large curvature in the vicinity of the centrosymmetric axis. On the contrary, the mesa-like structure at the center of the LP$_{30}$-LOS imparts diminutive refraction to rays with small θ_{sub}, resulting in a very high normal emission.

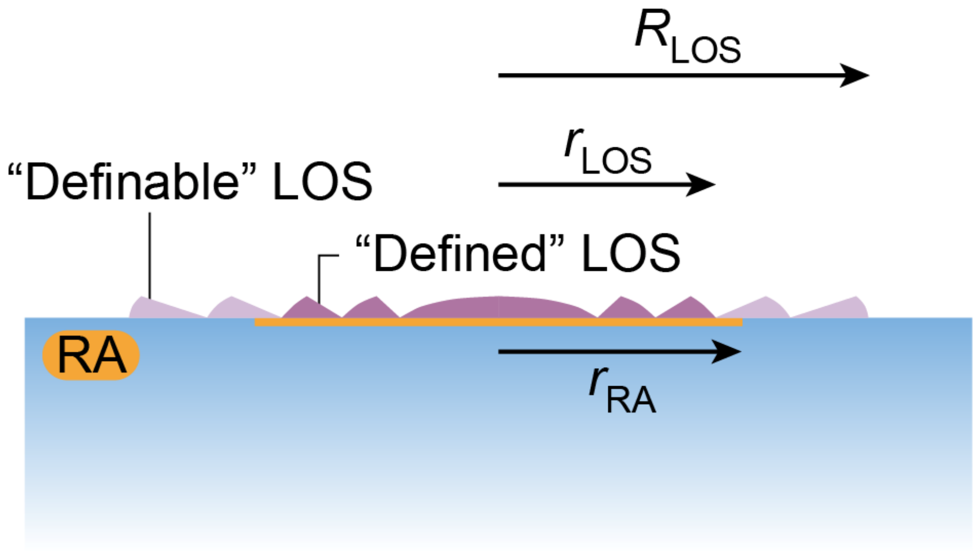

Supplementary Figure 9. The relationship among the maximal radius of LOS (R_{LOS}), the radius of the RA (r_{RA}), and the practical radius of LOS (r_{LOS}).

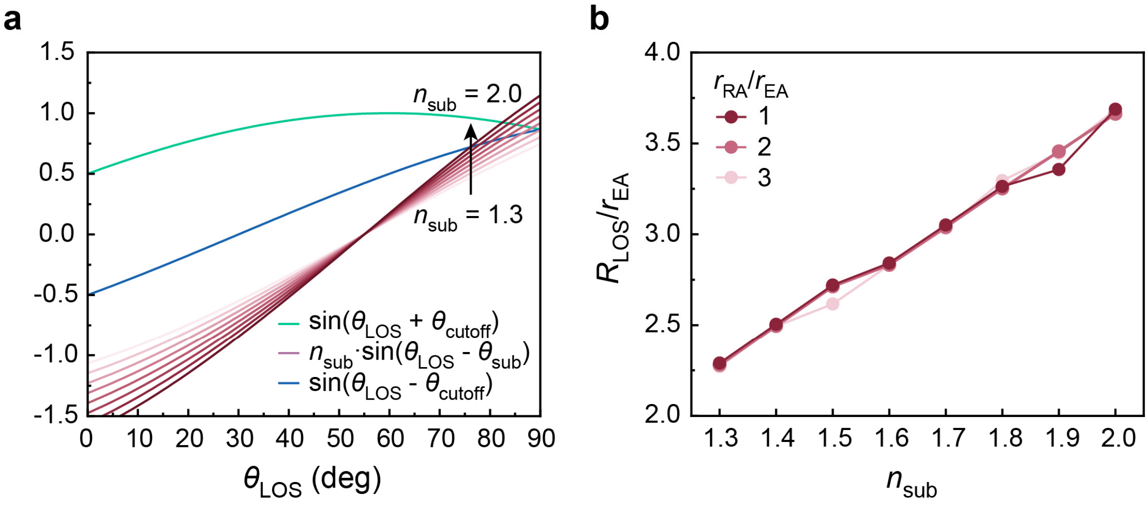

Supplementary Figure 10. Two-dimensional conditions on the maximal r_{LOS} regarding n_{sub} for the LOSs with lowpass weighting functions with its cutoff angle of θ_{cutoff}. For $\theta_{\mathrm{LOS}}(r) = \left|\tan^{-1}\frac{d}{dr}z(r)\right|$, its existence is secure only if there exists θ_{sub} such that $\sin(\theta_{\mathrm{LOS}}(r) - \theta_{\mathrm{cutoff}}) \leq n_{\mathrm{sub}} \cdot \sin(\theta_{\mathrm{LOS}} - \theta_{\mathrm{sub}}) \leq \sin(\theta_{\mathrm{LOS}}(r) + \theta_{\mathrm{cutoff}})$. (a) Given $\theta_{\mathrm{sub}} = 55°$ and $\theta_{\mathrm{cutoff}} = 30°$, a higher n_{sub} enables broader existence and window of θ_{LOS}. (b) Given $t_{\mathrm{sub}}/r_{\mathrm{EA}} = 1.4$ and $\theta_{\mathrm{cutoff}} = 30°$, the maximal r where θ_{LOS} exists ($\max r_{\mathrm{LOS}}$) increases monotonically with n_{sub}.

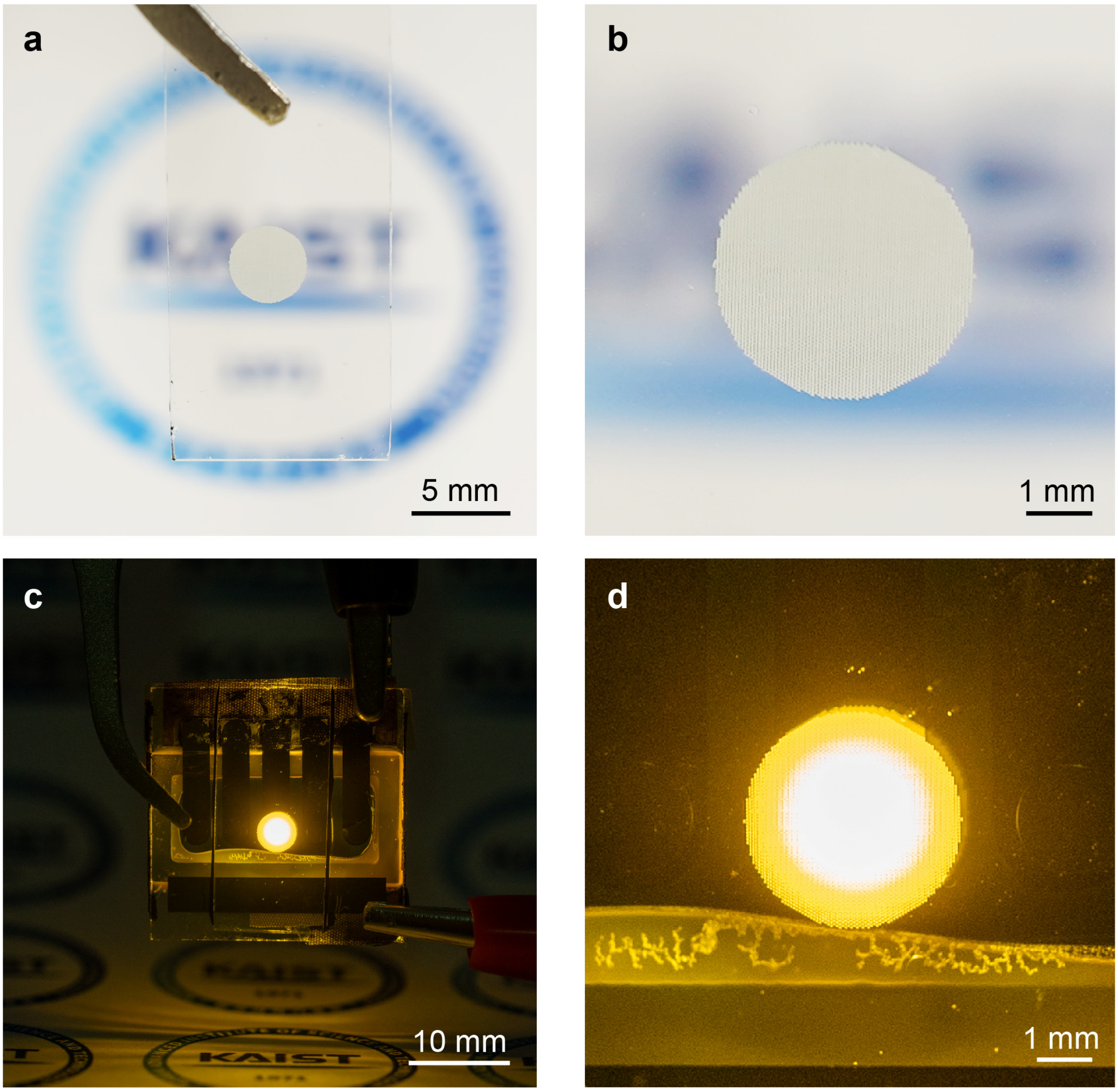

Supplementary Figure 11. MLA printed on top of a carrier glass ($r_{\mathrm{LOS}} = 2$ mm), and its combination with an OLED. (a) MLA pattern printed on a carrier glass, (b) its close-up image, (c) OLED with the MLA attached on top, (d) its close-up image. For an OLED with $r_{\mathrm{EA}} =$ 1 mm, the MLA showed optical artifacts and blurring owing to the edges of the MLA.

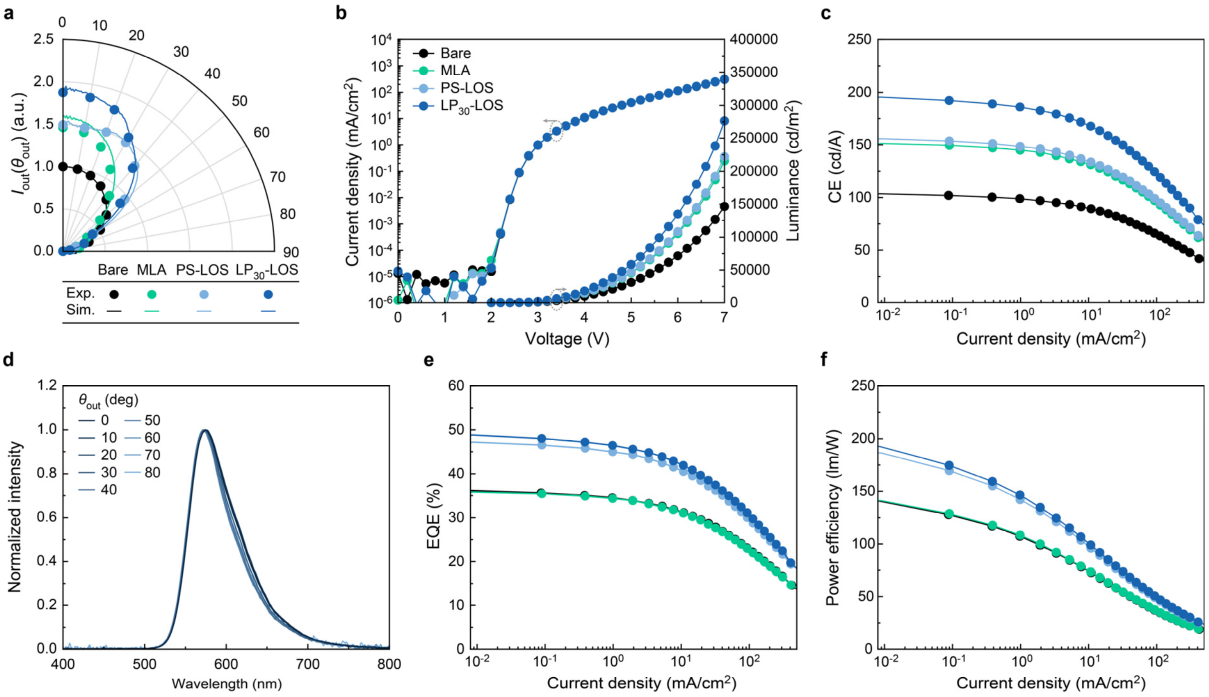

Supplementary Figure 12. The performance of the OLED with its d_{ETL} and d_{HTL} respectively of 50 nm and 50 nm. (a-c) The angular emission intensity (a), $J-V-L$ relationship (b), and CE (c) of the OLEDs with and without MLA, PS-LOS, and LP$_{30}$-LOS. (d) Angular electroluminescence spectrum of the OLED with LP$_{30}$-LOS. (e, f) EQE (e) and power efficiency (f) of the OLEDs with and without MLA, PS-LOS, and LP$_{30}$-LOS. Here, the LP$_{30}$-LOS is optimized to an OLED whose d_{ETL} and d_{HTL} are both 50 nm.

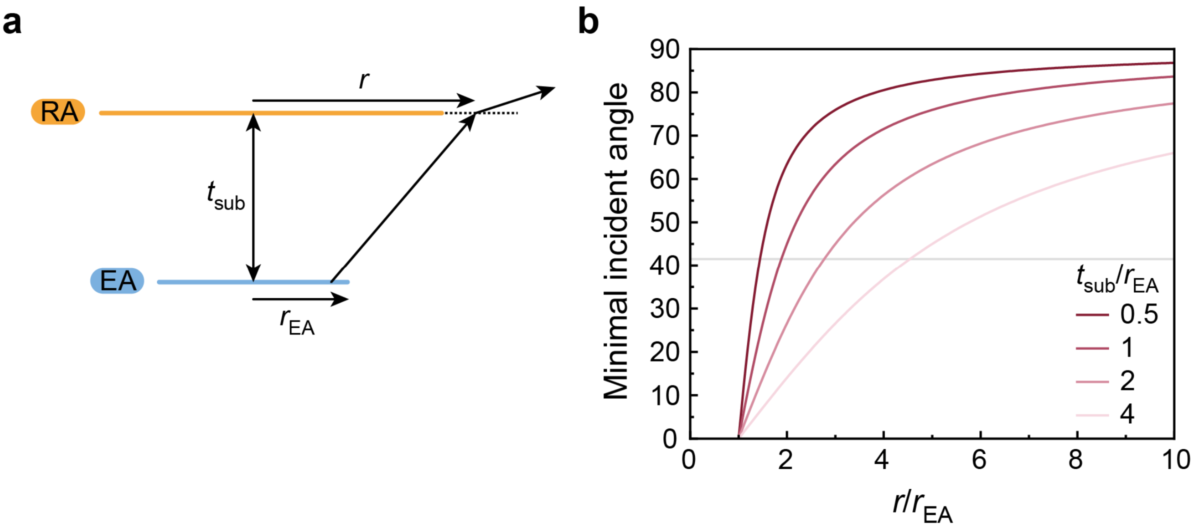

Supplementary Figure 13. The contribution of the ex-LOS region to the performance of the OLED. (a) A ray diagram and (b) the minimal incident angle available for different geometries. If the r/r_{EA} where the minimal incident angle equates the critical angle at the substrate-air interface is larger than $r_{\mathrm{LOS}}/r_{\mathrm{EA}}$, then ex-LOS region can contribute to the performance of the OLED.

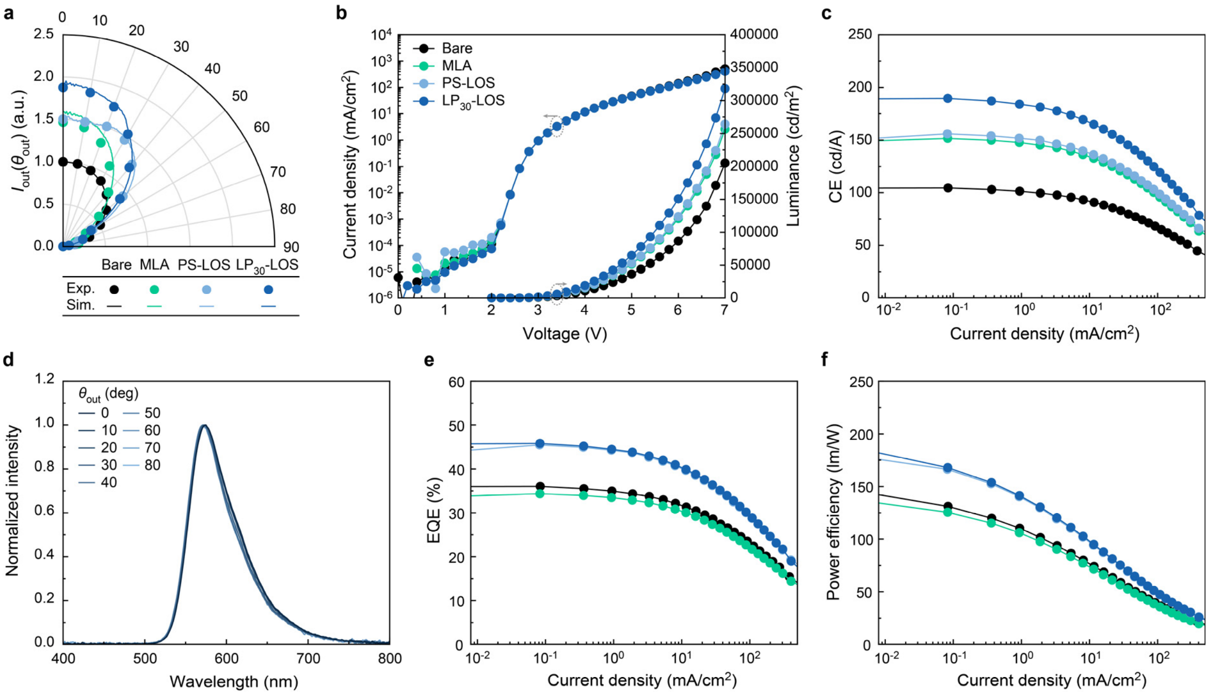

Supplementary Figure 14. The performance of the OLED with its d_{ETL} and d_{HTL} respectively of 50 nm and 30 nm. (a-c) The angular emission intensity (a), $J-V-L$ relationship (b), and CE (c) of the OLEDs with and without MLA, PS-LOS, and LP$_{30}$-LOS. (d) Angular electroluminescence spectrum of the OLED with LP$_{30}$-LOS. (e, f) EQE (e) and power efficiency (f) of the OLEDs with and without MLA, PS-LOS, and LP$_{30}$-LOS. Here, the LP$_{30}$-LOS is optimized to an OLED whose d_{ETL} and d_{HTL} are both 50 nm.

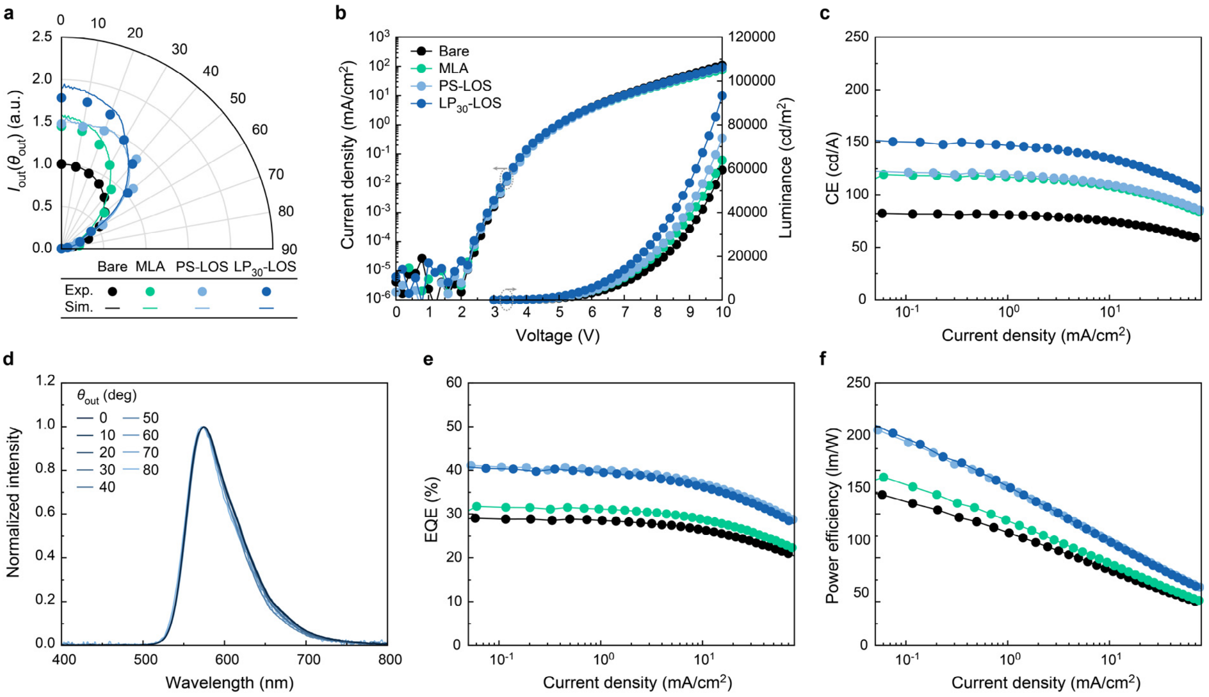

Supplementary Figure 15. The performance of the OLED with its d_{ETL} and d_{HTL} respectively of 70 nm and 140 nm. (a-c) The angular emission intensity (a), $J-V-L$ relationship (b), and CE (c) of the OLEDs with and without MLA, PS-LOS, and LP$_{30}$-LOS. (d) Angular electroluminescence spectrum of the OLED with LP$_{30}$-LOS. (e, f) EQE (e) and power efficiency (f) of the OLEDs with and without MLA, PS-LOS, and LP$_{30}$-LOS. Here, the LP$_{30}$-LOS is optimized to an OLED whose d_{ETL} and d_{HTL} are both 50 nm.

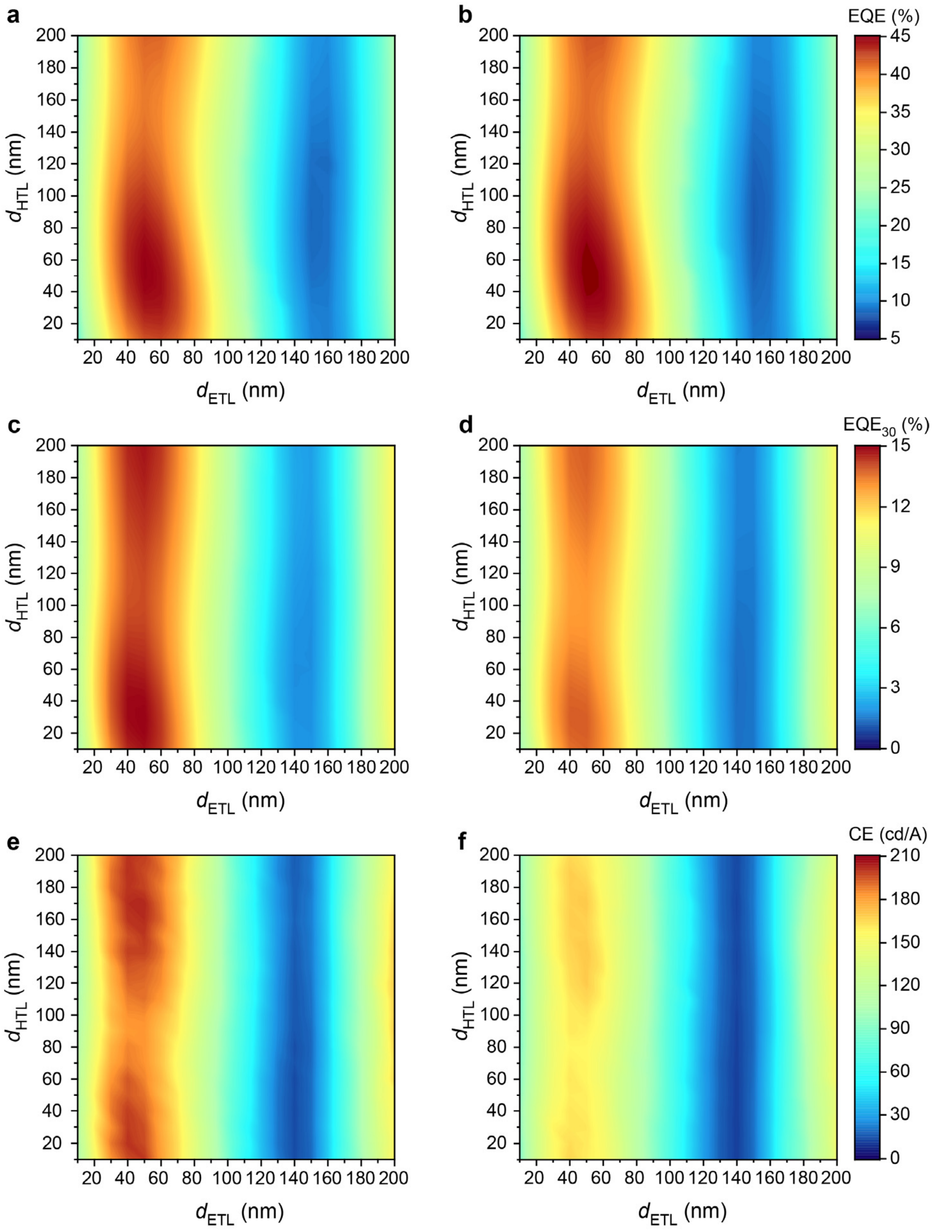

Supplementary Figure 16. Simulated performance of OLEDs with optimized LOSs. (a) EQE of LP30-LOS-attached OLEDs. (b) EQE of UH-LOS-attached OLEDs. (c) EQE_{30} of LP30-LOS-attached OLEDs. (d) EQE_{30} of UH-LOS-attached OLEDs. (e) CE of LP30-LOS-attached OLEDs. (f) CE of UH-LOS-attached OLEDs. Both LP30-LOS and UH-LOS were optimized to $I_{\mathrm{to-sub}}(\theta_{\mathrm{sub}})$ of the OLED with each d_{ETL} and d_{HTL} at a given $n_{\mathrm{sub}} = 1.51$, $t_{\mathrm{sub}}/r_{\mathrm{EA}} = 1.4$, $t_{\mathrm{LOS}}/r_{\mathrm{EA}} = 0.05$, and $\max r_{\mathrm{LOS}}/r_{\mathrm{EA}} = 2$.

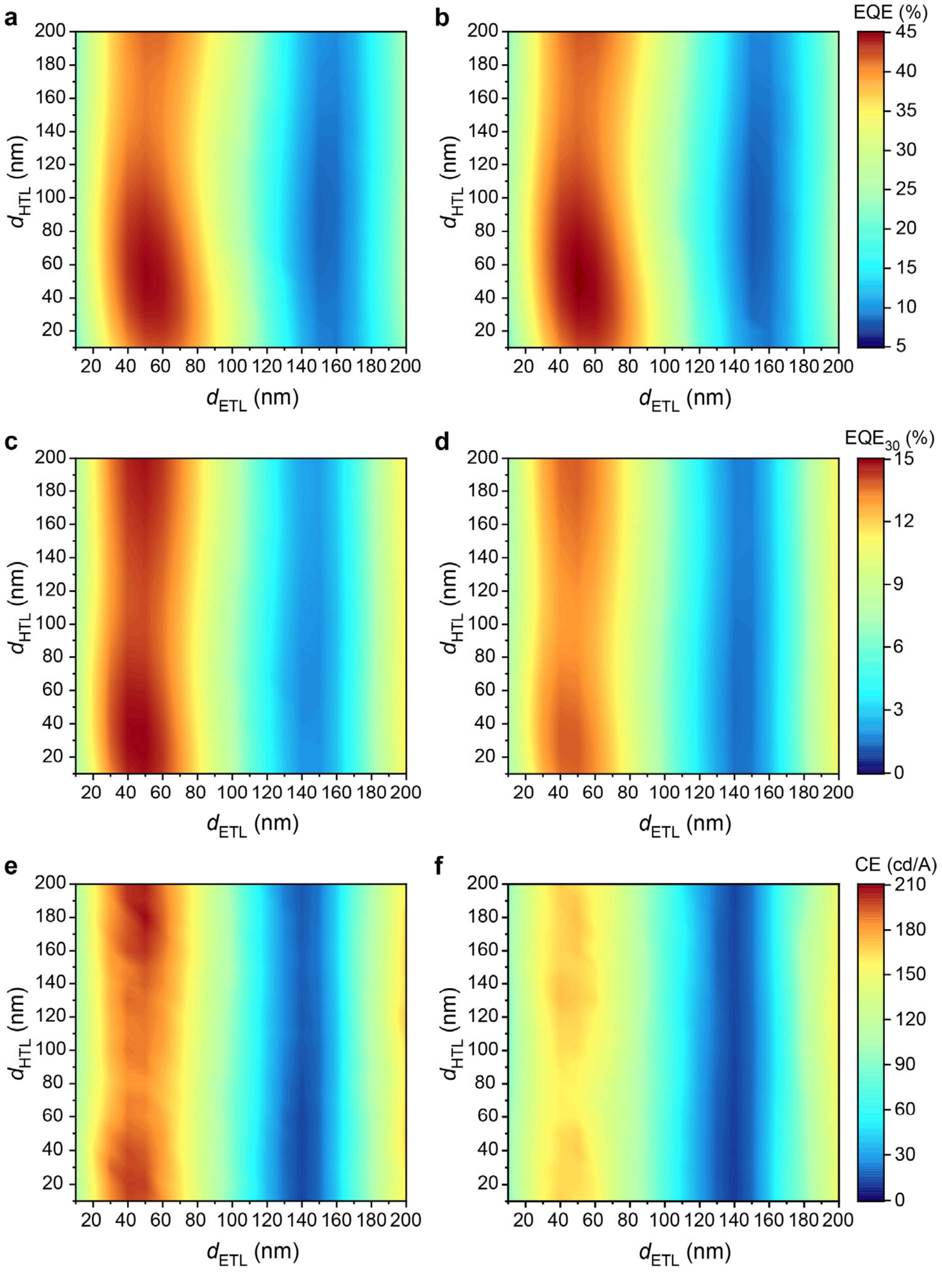

Supplementary Figure 17. Simulated performance of OLEDs with fixed LOSs. (a) EQE of LP30-LOS-attached OLEDs. (b) EQE of UH-LOS-attached OLEDs. (c) EQE_{30} of LP30-LOS-attached OLEDs. (d) EQE_{30} of UH-LOS-attached OLEDs. (e) CE of LP30-LOS-attached OLEDs. (f) CE of UH-LOS-attached OLEDs. Both LP30-LOS and UH-LOS were optimized to $I_{\mathrm{to-sub}}(\theta_{\mathrm{sub}})$ of the OLED with $d_{\mathrm{ETL}} = d_{\mathrm{HTL}} = 50\ \mathrm{nm}$ at a given $n_{\mathrm{sub}} = 1.51$, $t_{\mathrm{sub}}/r_{\mathrm{EA}} = 1.4$, $t_{\mathrm{LOS}}/r_{\mathrm{EA}} = 0.05$, and $\max r_{\mathrm{LOS}}/r_{\mathrm{EA}} = 2$.

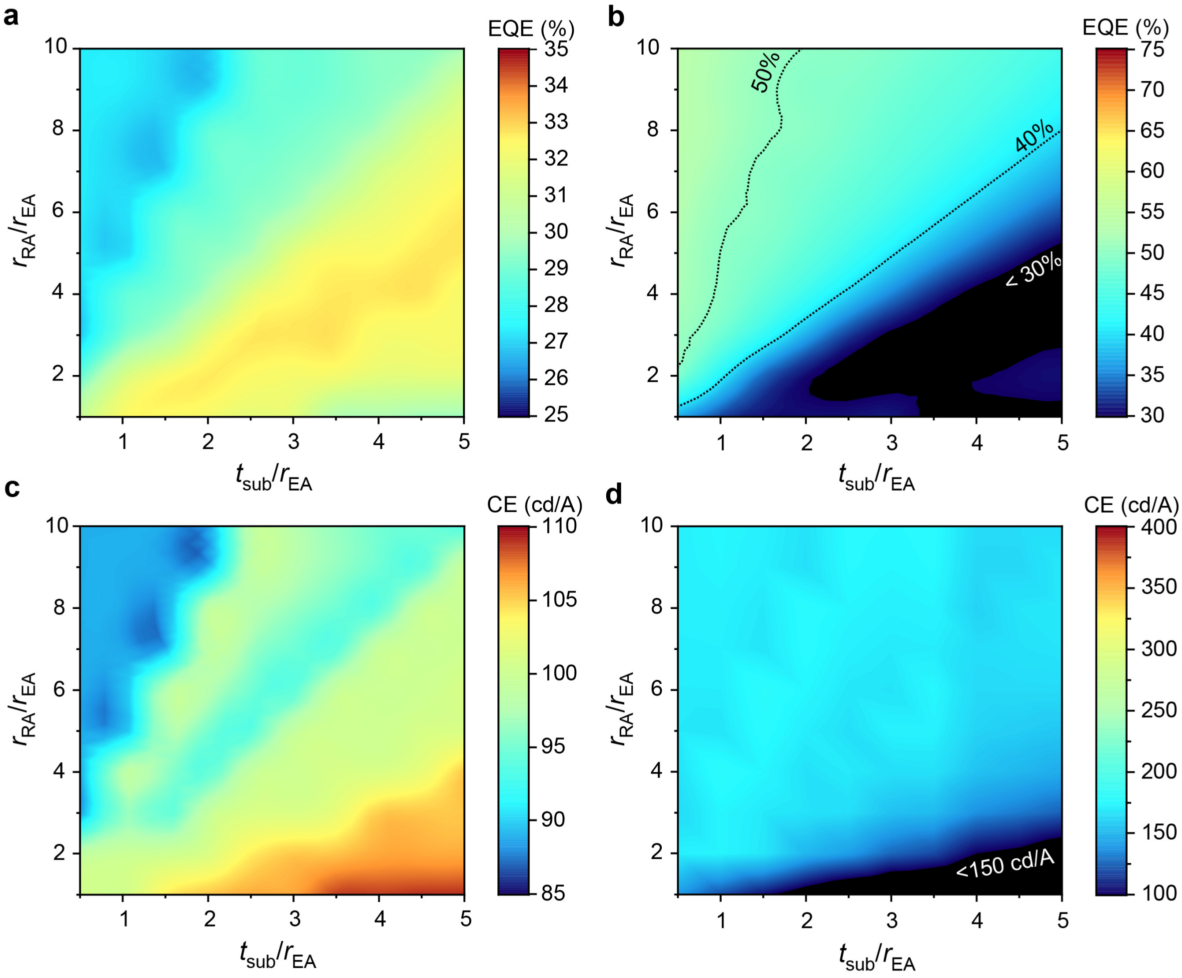

Supplementary Figure 18. Trans-scale optical simulations for OLEDs with their structures optimized for each geometric condition. (a) EQE of bare OLEDs, (b) EQE of MLA-attached OLEDs, (c) CE of bare OLEDS, and (d) CE of MLA-attached OLEDs. Here, n_{sub} and $t_{\mathrm{LOS}}/r_{\mathrm{EA}}$ were respectively remained at 1.51 and 1.4.

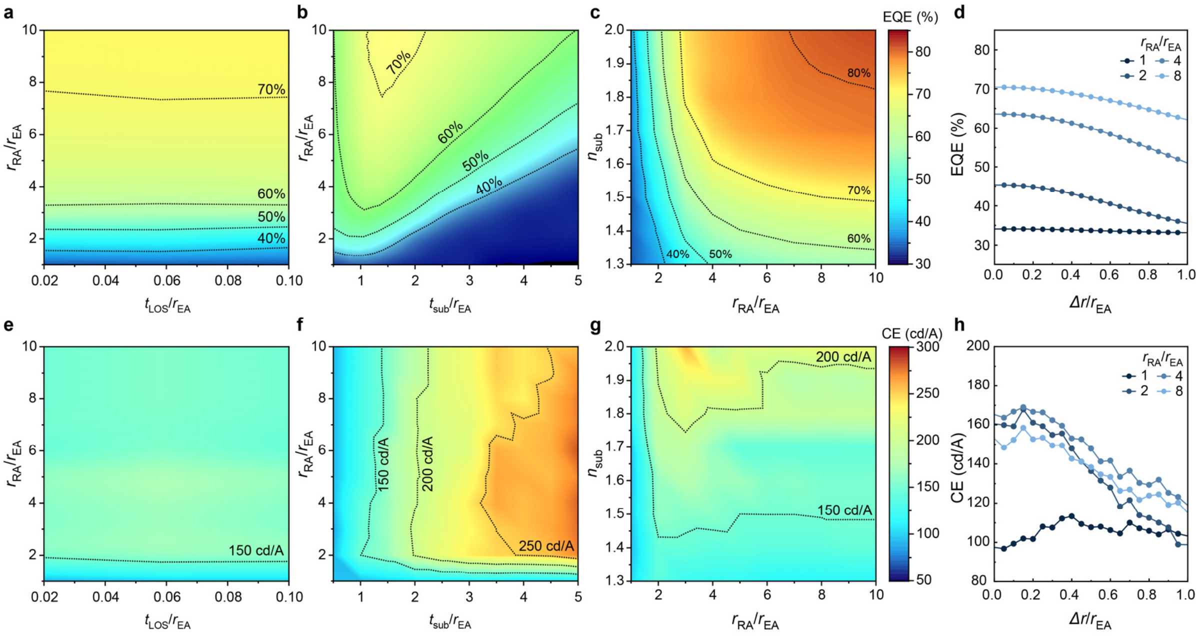

Supplementary Figure 19. Trans-scale optical simulations for OLEDs with their structures and the attached UH-LOSs optimized for each geometric condition. (a) EQE and (b) CE of the OLEDs with UH-LOSs with different $r_{\mathrm{RA}}/r_{\mathrm{EA}}$ and $t_{\mathrm{LOS}}/r_{\mathrm{EA}}$. Here, n_{sub} and $t_{\mathrm{sub}}/r_{\mathrm{EA}}$ are fixed to 1.51 and 1.4, respectively. (c) EQE and (d) CE of the OLEDs with UH-LOSs with different $r_{\mathrm{RA}}/r_{\mathrm{EA}}$ and $t_{\mathrm{sub}}/r_{\mathrm{EA}}$. Here, n_{sub} and $t_{\mathrm{LOS}}/r_{\mathrm{EA}}$ are fixed to 1.51 and 0.05, respectively. (e) EQE and (f) CE of the OLEDs with UH-LOSs with different n_{sub} and $r_{\mathrm{RA}}/r_{\mathrm{EA}}$. Here, $t_{\mathrm{LOS}}/r_{\mathrm{EA}}$ and $t_{\mathrm{sub}}/r_{\mathrm{EA}}$ are fixed to 0.05 and 1.4, respectively. (g, h) The impact of the in-plane misalignment to the (g) EQE and (h) CE of the OLEDs with UH-LOSs. Here, $t_{\mathrm{sub}}/r_{\mathrm{EA}}$, $t_{\mathrm{LOS}}/r_{\mathrm{EA}}$, and n_{sub} are fixed to 1.4, 0.05, and 1.51, respectively.

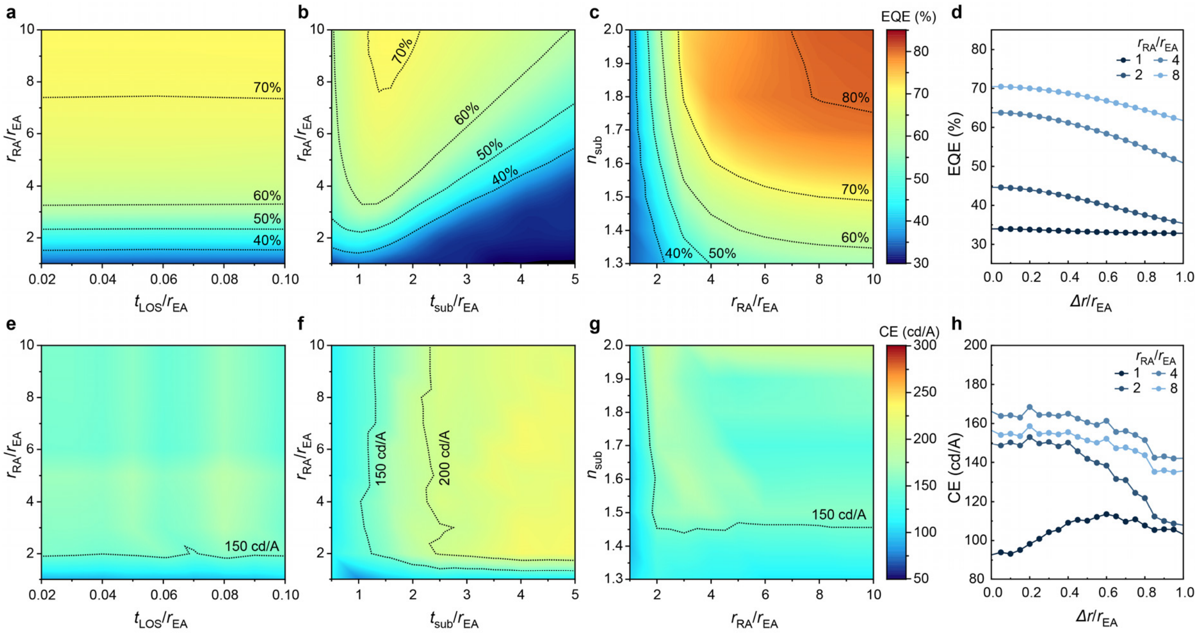

Supplementary Figure 20. Trans-scale optical simulations for OLEDs with their structures and the attached PS-LOSs optimized for each geometric condition. (a) EQE and (b) CE of the OLEDs with PS-LOSs with different $r_{\mathrm{RA}}/r_{\mathrm{EA}}$ and $t_{\mathrm{LOS}}/r_{\mathrm{EA}}$. Here, n_{sub} and $t_{\mathrm{sub}}/r_{\mathrm{EA}}$ are fixed to 1.51 and 1.4, respectively. (c) EQE and (d) CE of the OLEDs with PS-LOSs with different $r_{\mathrm{RA}}/r_{\mathrm{EA}}$ and $t_{\mathrm{sub}}/r_{\mathrm{EA}}$. Here, n_{sub} and $t_{\mathrm{LOS}}/r_{\mathrm{EA}}$ are fixed to 1.51 and 0.05, respectively. (e) EQE and (f) CE of the OLEDs with PS-LOSs with different n_{sub} and $r_{\mathrm{RA}}/r_{\mathrm{EA}}$. Here, $t_{\mathrm{LOS}}/r_{\mathrm{EA}}$ and $t_{\mathrm{sub}}/r_{\mathrm{EA}}$ are fixed to 0.05 and 1.4, respectively. (g, h) The impact of the in-plane misalignment to the (g) EQE and (h) CE of the OLEDs with PS-LOSs. Here, $t_{\mathrm{sub}}/r_{\mathrm{EA}}$, $t_{\mathrm{LOS}}/r_{\mathrm{EA}}$, and n_{sub} are fixed to 1.4, 0.05, and 1.51, respectively.

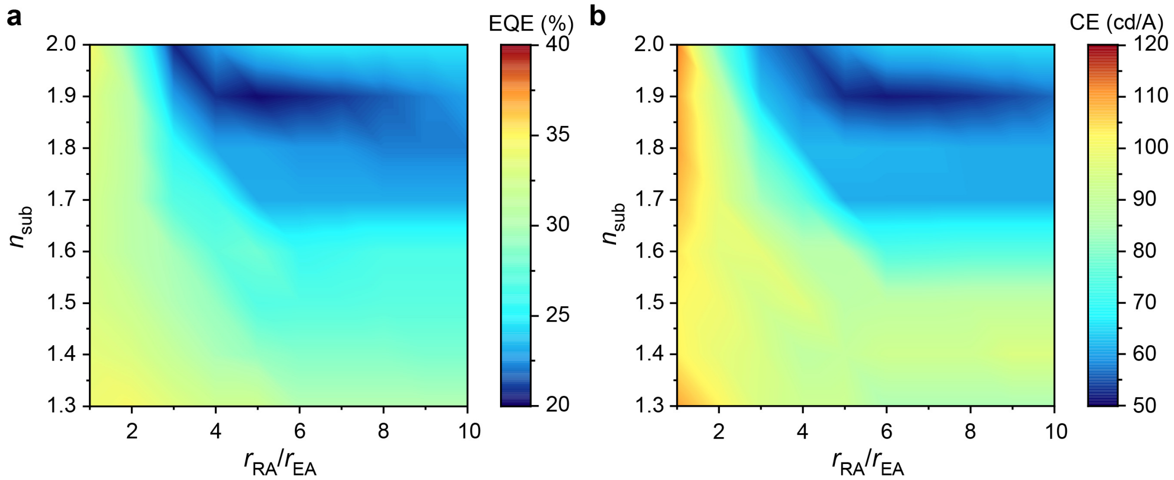

Supplementary Figure 21. Simulated performance of bare OLEDs optimized for different aperture radius ratios. (a) EQE and (b) CE of the OLEDs optimized to variable n_{sub} and $r_{\mathrm{RA}}/r_{\mathrm{EA}}$ and fixed $t_{\mathrm{sub}}/r_{\mathrm{EA}} = 1.4$.

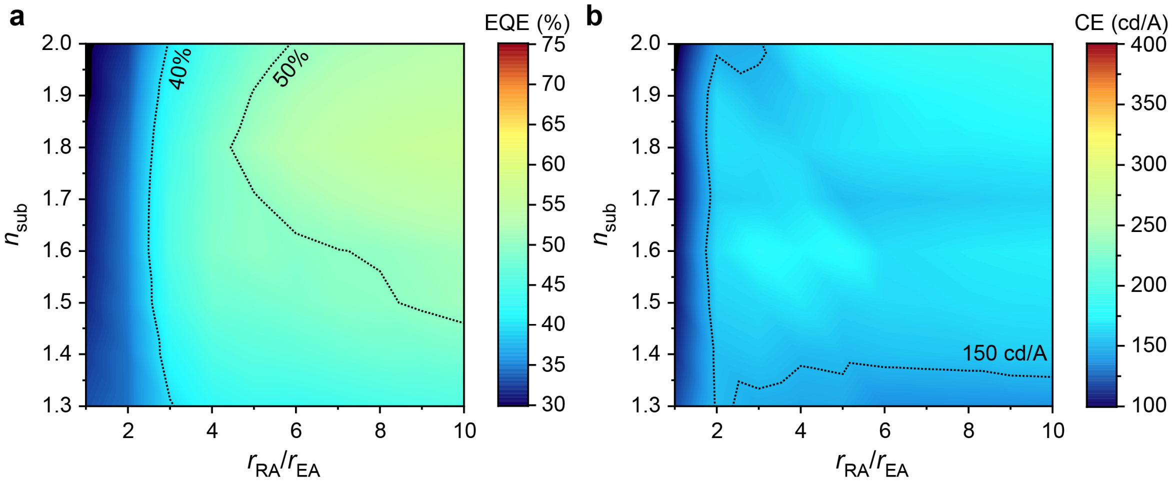

Supplementary Figure 22. Simulated performance of MLA-attached OLEDs optimized for different aperture radius ratios. (a) EQE and (b) CE of the OLEDs optimized to variable n_{sub} and $r_{\mathrm{RA}}/r_{\mathrm{EA}}$ and fixed $t_{\mathrm{sub}}/r_{\mathrm{EA}} = 1.4$ and $t_{\mathrm{LOS}}/r_{\mathrm{EA}} = 0.05$.

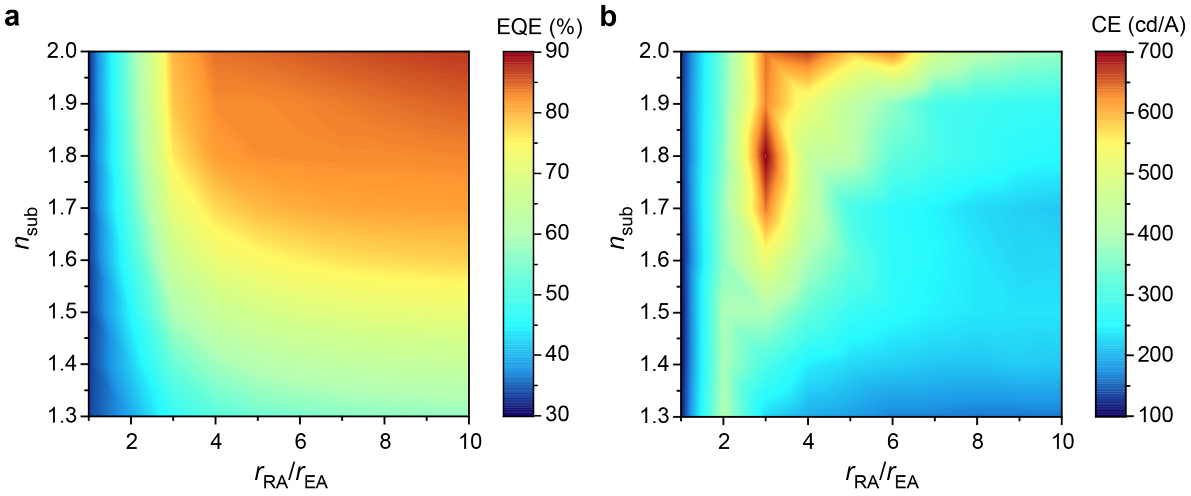

Supplementary Figure 23. Simulated performance of macroscale half-ball-attached OLEDs optimized for different aperture radius ratios. (a) EQE and (b) CE of the OLEDs optimized to variable n_{sub} and $r_{\mathrm{RA}}/r_{\mathrm{EA}}$ and fixed $t_{\mathrm{sub}}/r_{\mathrm{EA}} = 1.4$.

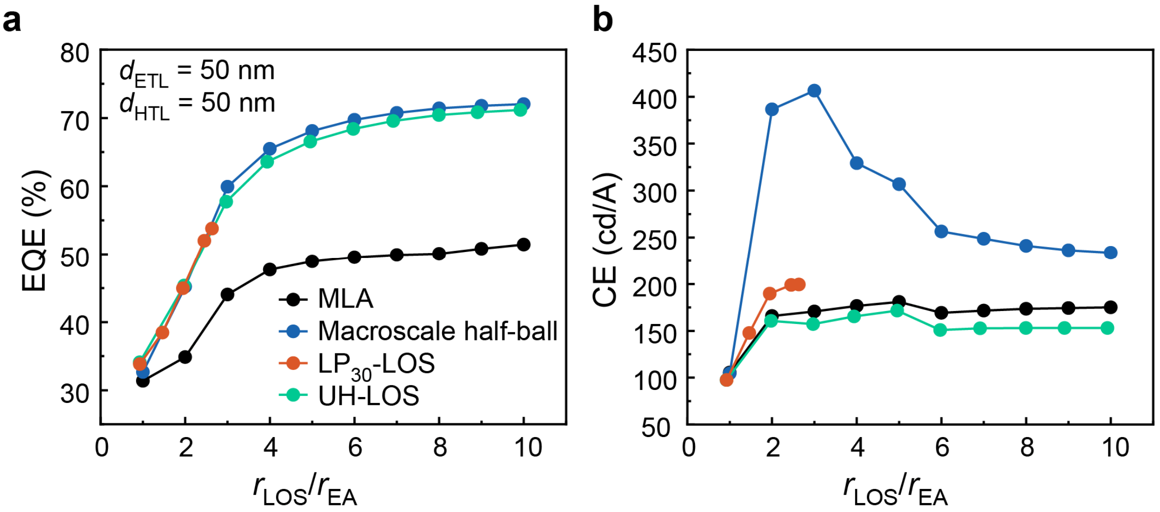

Supplementary Figure 24. Simulated performance of OLEDs with various external outcoupling structures attached. (a) EQE abd (b) CE. Here, the OLED was fixed to have $d_{\mathrm{ETL}} = d_{\mathrm{HTL}} = 50$ nm, and n_{sub}, $t_{\mathrm{sub}}/r_{\mathrm{EA}}$, and $t_{\mathrm{LOS}}/r_{\mathrm{EA}}$ are respectively set to 1.51, 1.4, and 0.05. Because of the limited R_{LOS}, the EQE and CE of the LP_{30}-LOS-attached OLED were delimited to 53.79% and 199.3 cd/A, respectively, at the $r_{\mathrm{LOS}}/r_{\mathrm{EA}} = 2.633$.

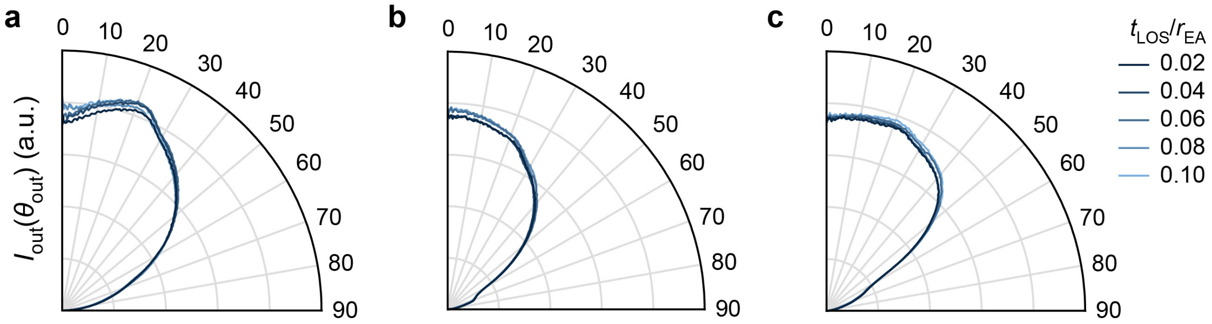

Supplementary Figure 25. Simulated angular emission intensity of the OLEDs with LP_{30}-LOS with its $r_{\mathrm{RA}}/r_{\mathrm{EA}}$ of (a) 1, (b) 2, and (c) 3. For each case, $t_{\mathrm{LOS}}/r_{\mathrm{EA}}$ has negligible impact on $I_{\mathrm{out}}(\theta_{\mathrm{out}})$.

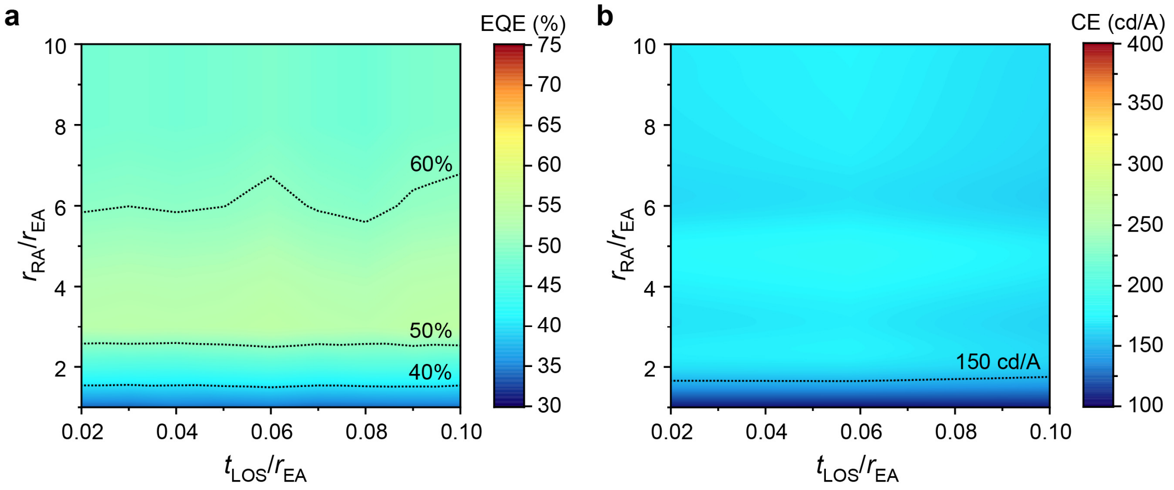

Supplementary Figure 26. Simulated negligible impact of t_{LOS} on the performance of MLA-attached OLED. (a) EQE and (b) CE. In both cases, $t_{\mathrm{sub}}/r_{\mathrm{EA}} = 1.4$ and $n_{\mathrm{sub}} = 1.51$.

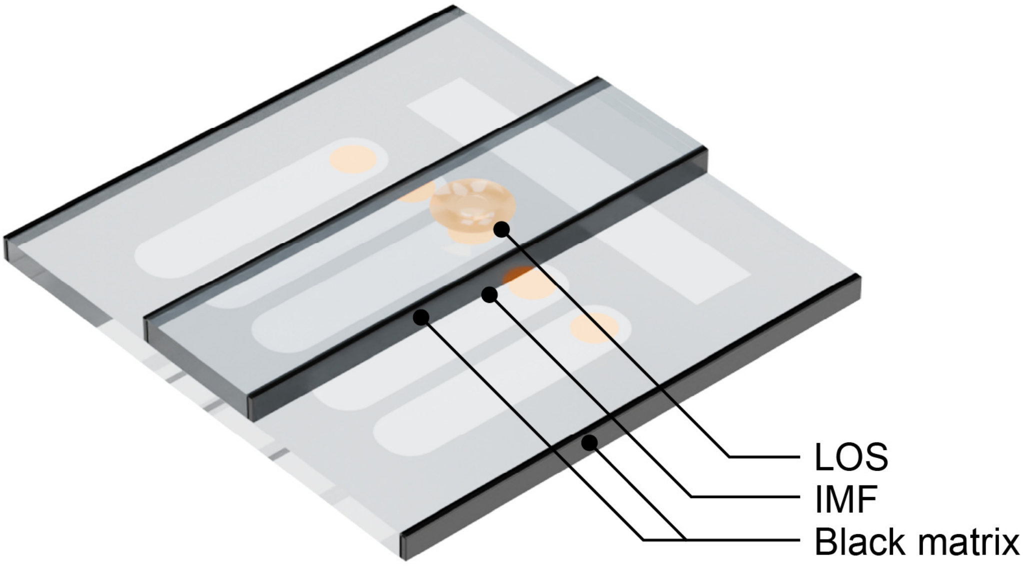

Supplementary Figure 27. The OLED measurement setup. The side faces of both LOS-carrying glass and the substrate were blocked with a black matrix so that no substrate mode is extracted into air mode through the faces. The LOS-carrying glass and the substrate were optically cemented with an index-matching fluid (IMF) with a refractive index of 1.51.